Supporting Information

How can infra-red excitation both accelerate and slow charge transfer in the same molecule?

Zheng Ma[†], Zhiwei Lin[§], Candace M. Lawrence[@], Igor V. Rubtsov[§*], Panayiotis Antoniou[¶], Spiros S. Skourtis[¶*], Peng Zhang[†*], David N. Beratan[†‡||*]

[†]Department of Chemistry, Duke University, Durham, North Carolina 27708, United States
[‡]Department of Physics, Duke University, Durham, North Carolina 27708, United States
[||]Department of Biochemistry, Duke University, Durham, North Carolina 27708, United States
[§]Department of Chemistry, Tulane University, New Orleans, Louisiana, 70118
[¶]Department of Physics, University of Cyprus, Nicosia 1678, Cyprus
[@]Department of Chemistry, Xavier University of Louisianan, New Orleans, Louisiana, 70125

I. EXPERIMENTAL DETAILS

I.1 TRANSIENT FEMTOSECOND SPECTROMETER

Laser beams of various wavelengths required for the experiments were generated using a regenerative amplifier (Spitfire, Spectra Physics) seeded by a Ti:sapphire oscillator (Vitesse, Coherent Inc.) producing pulses at 806 nm with ca. 45 fs duration. The output beam was split into two nearly equal parts. One beam was used to generate mid-IR pulses via optical parametric amplification (Type-II mixing in a 3 mm thick BBO, β-BaB_2O_4, crystal) followed by a difference frequency generation (Type-I mixing in a 2 mm thick $AgGaS_2$ crystal). Mid-IR pulses at ca. 6 μm had ca. 1.5 μJ/pulse energy and ca. 140 cm^{-1} spectral width.[1-2] The second part of the Ti:S output was split into two parts: a small fraction (~2 μJ/pulse) was used to generate white light in a 2 mm thick sapphire wafer and the rest was used to produce a second harmonic in a 2 mm thick BBO crystal. The mid-IR, white-light, and UV (403 nm) pulses were focused onto the sample with lenses of 100, 150, and 400 mm focal length, respectively.

The probe beams, either the white-light or mid-IR, were introduced into an image spectrometer (Triax-190, Jobin Yvon, Inc.) equipped with two detectors attached to its two output ports. A single-channel HgCdTe detector (Infrared Associates) connected to a box-car integrator was used to measure mid-IR intensities. A linear CCD array with 2048 channels was used for recording transient spectra in the visible range at 1 kHz repetition rate.

Several types of measurements were performed, such as UV-pump / Vis-probe, UV-pump / IR probe, and UV-pump / IR-pump / Vis-probe. The polarizations of the mid-IR and visible pulses were controlled with pairs of a half-wave plates and polarizers. The total $\tau + T$ time delay available in the 3-pulse measurements was limited by ca. 110 ps.

I.2 SAMPLE PREPARATION

The electron donor, 8-(4′′-*N,N*-Dimethylanilinyl)-9-[2′,3′,5′-tri-*O*-(*tert*-butyldimethylsilyl) ribofuranosidyl]-2-aminopurin-6-one (D) and electron acceptor, 4-Amino-5-[2′′-(9′′′-anthracenyl)ethynyl]-1-[2′,3′,5′-tri-*O*-(*tert*-butyldimethylsilyl)-ribofuranosidyl]pyrimidin-4-one (A) (Scheme 1a), were synthesized according to the reported procedure.[3] The association constant for guanosine-cytidine (GC) base-pairing in dichloromethane (DCM) solution is ca. 3.8×10^4 M^{-1}.[4] To minimize the amount of unbound acceptor in the sample, all time-resolved measurements were performed in the mixtures with 5-fold molar excess of the donor over the acceptor, at ca. 75 and 15 mM concentrations, respectively. The measurements were performed under N_2 atmosphere in an all-Teflon flow cell with an optical pathlength of 130 μm and windows made of BaF_2.

I.3 ADDITIONAL EXPERIMENTAL RESULTS

Excited and charge separated state transient UV-pump / Vis-probe spectra of DMA-GC-Anth.

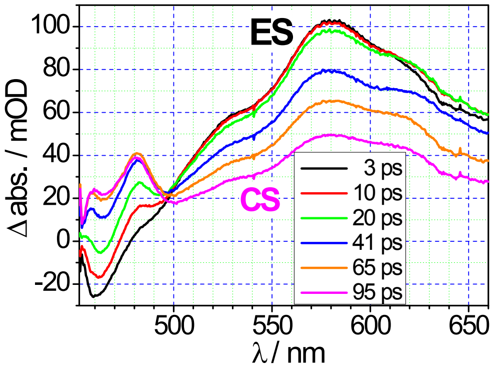

Figure. S1. UV-pump / Vis-probe transient spectra of DMA-GC-Anth in DCM measured at various delays (see inset) following excitation at 400 nm. EE is the acceptor localized electronic excited state. CS is the charge separated state.

I.4 QUANTUM YIELD OF CS, MEASURED BY UV-PUMP / IR-PROBE SPECTROSCOPY

UV-pump / IR-probe measurements were performed to evaluate independently the quantum yield of charge separation and to evaluate the changes in transition dipole strength of the involved vibrational modes in states of the compound (EE and CS). The latter values were used to evaluate the probabilities of vibrational excitation in the 3-pulse experiments. Note that in the 3-pulse measurements the IR pulses excite DBA either in the electronically excited state or in the CS state. It is therefore necessary to understand the changes in the frequencies and IR strengths for the modes at the bridge in both electronically-excited and CS states and compare them to those relevant for the ground electronic state.

Transient UV-pump / IR-probe spectra measured at time delays of 5.7 and 106 ps, are shown in Fig. S2. As inspection of this figure reveals, both main IR peaks (at 1650, 1688 cm^{-1}) shift to lower frequencies upon excitation, in both the electronically-excited (delay of 5.7 ps) and in the CS states (delay of 106 ps). Moreover, for both peaks, the transition dipoles in the excited state are stronger than those in the ground state (as the absorption features peaking at 1683 and 1635 cm^{-1} are bigger than the bleach peaks at 1697 and 1655 cm^{-1}). A fit of the data using the kinetic scheme of Fig. 3 in main text and Gaussian spectral shapes (thin red lines in Fig. S2) yields the following results for the frequencies ($\bar{\nu}$) and transition dipoles (μ) squared for the antisymmetric stretching mode at 1688 cm^{-1}: $\bar{\nu}_{CO\ as.}(EE) = 1684.9$ cm^{-1}, $\bar{\nu}_{CO\ as.}(CS) = 1685.0$ cm^{-1}, $\mu^2_{CO\ as.}(G)$ / $\mu^2_{CO\ as.}(EE)$ / $\mu^2_{CO\ as.}(CS) = 1 : (1.1 \pm 0.1) : (0.78 \pm 0.1)$.

The modeling of the transients associated with the peak at 1650 cm^{-1} is less certain as the peak comprises three transitions, which are not spectrally resolved. Nevertheless, the total transition dipole squared ($\mu_t^2 = \sum_i \mu_i^2$, where the summation is performed over the three modes that make the peak) for the peak in G, EE, and CS states are related as: $\mu_t^2(G) : \mu_t^2(EE) : \mu_t^2(CS) = 1 : (1.8 \pm 0.2) : (1.25 \pm 0.1)$. Using these data the probabilities of vibrational excitation in the electronically excited and CS states were evaluated at 0.33 and 0.23, respectively.

The QY of CS can be obtained from the dynamics of the bleach peak at ca. 1695 cm^{-1}; at small time delays, it characterizes the amount of the excited states produced by UV, whereas at larger delays (106 ps) it reflects the amount of CS states formed. The modeling (shown in Fig. S2 as thin red lines) results in an estimated quantum yield for CS of 0.75 ± 0.25. Here, the large errors originate from a substantial overlap of the absorption and bleach features (shifted by only ca. 3 cm^{-1}), as well as from an uncertainty in the widths of the absorption peaks in the EE and CS states.

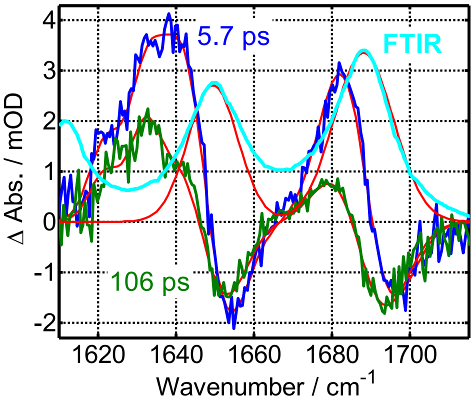

Figure. S2. Transient UV-pump / IR-probe spectra of DMA-GC-Anth at time delays of 5.7 ps (blue) and 106 ps (green) and scaled linear absorption spectrum (FTIR, cyan). The results of the global fit with four fundamental transitions (see text) are shown with red lines.

II. AB INITIO ANALYSIS OF ELECTRONIC STRUCTURE AND ET PARAMETERS IN DMA-GC-ANTH

II.1 ELECTRONIC STRUCTURE OF DMA-GC-ANTH

Ground state electronic structure and normal mode analysis were carried out using the Gaussian 09 software package[5] with density functional theory (B3LYP/6-31G(d, p)) and the PCM solvent model (in dichloromethane (DCM)). Excited-state characterization was performed using TD-DFT (TD-B3LYP(6-31G(d, p)) with the PCM solvation model. The B3LYP, cam-B3LYP, M06HF and wB97XD functionals were tested by comparing the character of the excited states and the vertical excitation energies with experiment.

Photo-induced charge transfer in DMA-GC-Anth is initiated by UV excitation of the alkyne and anthracene units. The vacancy created in the anthracene π orbital is filled by the electron from a DMA-G π orbital via a charge-separation reaction. Charge-recombination happens when the excited electron of alkyne-anthracene π^* moves to the DMA-G species to fill the hole. The charge-separation coupling is between the $\pi \rightarrow \pi^*$ local-excited state of alkyne-anthracene and the DMA-G $\pi \rightarrow$ Anth π^* state.

The computed and experimental vertical excitation energy for low-lying excited states are summarized in Table S1. At the TD-B3LYP level of theory, the first singlet excited state (S1) corresponds to the transition between the mixed HOMO of the DMA-G fragment and the LUMO of the alkyne-anthracene. The second excited state (S2) corresponds to a local excitation from the alkyne-anthracene HOMO to its LUMO. The calculated S2 vertical excitation energy occurs at 452 nm, which is consistent with the experimental data (~440nm). The nature of the S2 state was determined experimentally to be a $\pi \rightarrow \pi^*$ transition. The TD-B3LYP calculation correctly captured the excited state energy ordering. The cam-B3LYP, wB97XD and M06HF functionals were also used to describe the excited states but failed to produce the expected excited states localization and energetics. These results also appear in Table S1.

Table S1. Comparison of different density functionals on computed vertical excitation energies and excited state localizations for DMA-GC-Anth.

Functional	$E(S1)$	S1 Character	$E(S2)$	S2 Character
cam-B3LYP	404nm	alkyne-anthracene $\pi \rightarrow \pi^*$	312nm	alkyne-anthracene $\pi \rightarrow \pi^*$
B3LYP	479nm	DMA-G $\pi \rightarrow$alkyne-anthracene π^*	452nm	alkyne-anthracene $\pi \rightarrow \pi^*$
wB97XD	402nm	alkyne-anthracene $\pi \rightarrow \pi^*$	312nm	alkyne-anthracene $\pi \rightarrow \pi^*$
M06HF	362nm	cytidine / alkyne-anthracene $\pi \rightarrow \pi^*$	318nm	cytidine / alkyne-anthracene $\pi \rightarrow \pi^*$
Experiment	480nm	DMA-G $\pi \rightarrow$ alkyne-anthracene π^*	440nm	alkyne-anthracene $\pi \rightarrow \pi^*$

Table S2 shows the computed frontier orbital energies and their nature. The HOMO of DMA-GC-Anth is a π orbital that is a mixture of the highest occupied π orbital on guanosine (G) and the highest occupied π orbital on the DMA fragment. The LUMO of DMA-GC-Anth is largely the LUMO of alkyne-anthracene fragment. DFT calculation indicates that the HOMO-LUMO energy gaps for both the DMA-G fragment and the cytidine-alkyne-anthracene fragment are ~4-5eV, which makes hole transfer process more favorable than electron transfer.

Table S2. Energies and nature of frontier MOs of DMA-GC-Anth calculated by DFT B3LYP. Excited electronic state geometries are optimized using TD-DFT B3LYP.

MO Nature	Energy/eV at S0 Equilibrium Geometry	Energy/eV at S1 Equilibrium Geometry	Energy/eV at S2 Equilibrium Geometry
π(DMA-G)	-4.999	-4.459	-4.956
π^*(DMA-G)	-0.548	-0.563	-0.516
π(cytidine)	-6.353	-6.495	-6.394
π^*(cytidine)	-1.348	-1.507	-1.389
π(alkyne-anthracene)	-5.315	-5.235	-5.087
π^*(alkyne-anthracene)	-2.179	-2.429	-2.436

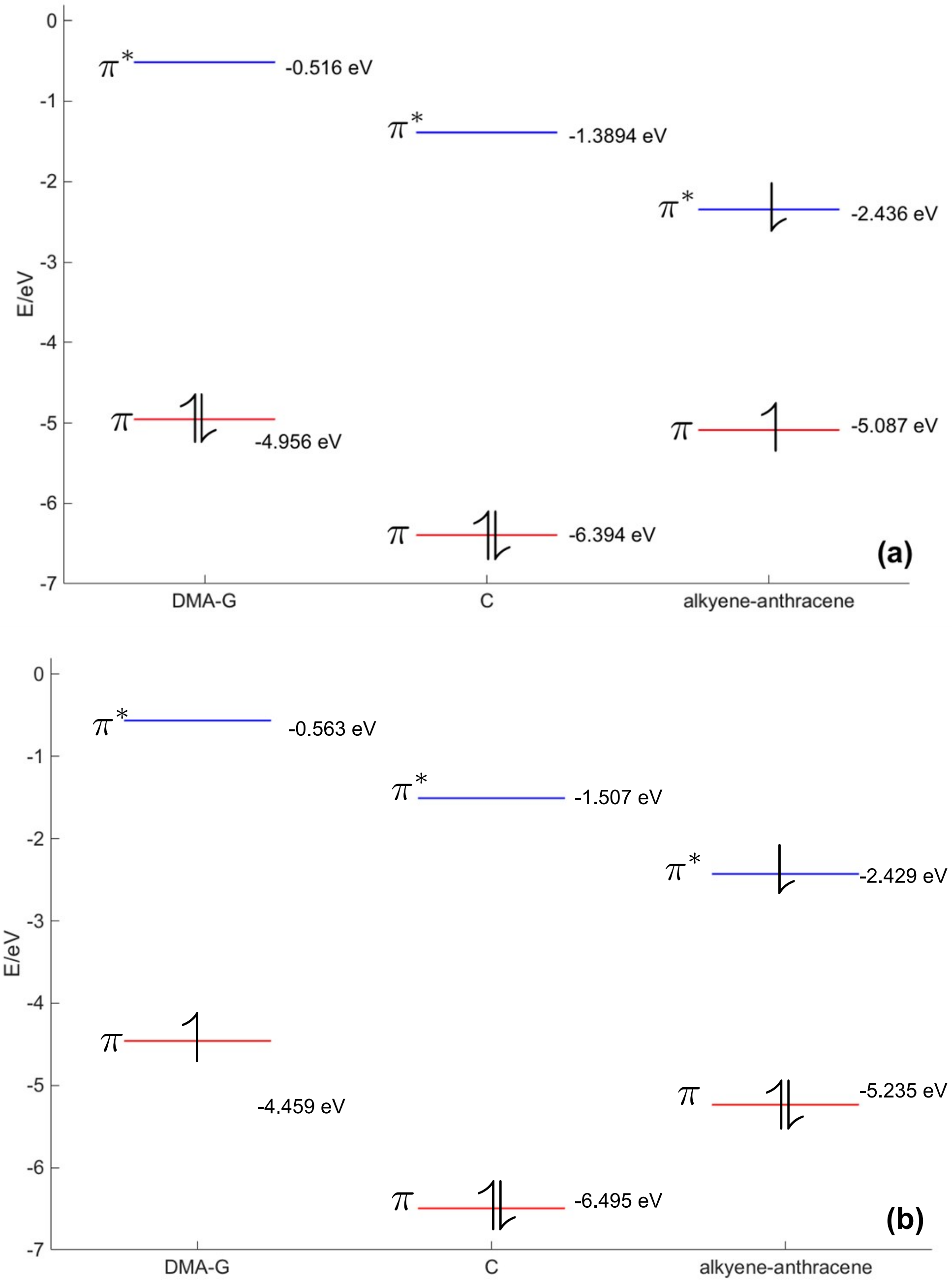

Scheme S1. Leading electronic configurations of: (a) S2 state at its optimized structure, and (b) S1 state at its optimized structure calculated by TD-DFT B3LYP.

The adiabatic energy difference (without zero point energy corrections) between the S1 and S2 states is 0.33 eV, while the gap between the S1 and ground states is 2.17eV. These numbers are consistent with experimental ΔG values for charge separation ($\Delta G = -0.41eV$) and recombination ($\Delta G = -2.5eV$). This consistency further confirms that the TD-B3LYP/6-31G(d,p) level of electronic structure theory is adequate. In the S1 equilibrium geometry, the energy difference between the S1 and S2 states is 0.67 eV. For the S2 equilibrium geometry, the state has mixed character of both charge transfer (guanosine / DMA $\pi\rightarrow$ alkyne-anthracene π^*) and a dominant local excitation (alkyne-anthracene $\pi\rightarrow\pi^*$). At the same S2 geometry, the S1 state has the opposite mixing character (charge transfer dominates) and the S1 state just 0.035eV lower than the S2 state. This ab initio data indicate that the transition from S2 to S1 has a very low activation barrier, consistent with conclusions derived from experiment[3, 6] (the reaction barrier was found to be ~0.09 eV).

In the S2 state equilibrium geometry, the structure in the H-bond region, including the three H-bond lengths, bond angles, dihedral angle between the guanosine and the cytidine planes, -NH_2 group bond angles, and the carbonyl group bond lengths, were not significantly changed (<1%) compared to the ground state equilibrium geometry. The geometric properties in the alkyne-anthracene fragment, including the C-C bond lengths of the anthracene rings, the carbon-carbon triple bond length, and the bond length between the alkyne group and the anthracene group, were not significantly changed either (<2%). The dihedral angle between the DMA plane and the guanosine plane also remains approximately the same. The only substantial geometry change is the dihedral angle between the anthracene plane and the cytidine plane. In the ground state equilibrium geometry, this dihedral angle is ~42° and in the S2 equilibrium geometry it is ~21°. This difference is caused by the local excitation of anthracene electron. However, in the S1 equilibrium geometry, the H-bond lengths decreased by ~10% and the DMA-guanosine dihedral angle decreased by ~15° compared to ground state equilibrium geometry. The anthracene-cytidine dihedral angle for the S1 equilibrium geometry is ~25°, which is similar to the dihedral angle in the S2 equilibrium geometry. The similarity between the S0 and the S2 equilibrium geometries indicates that the vibrational motion of the H-bonds is likely similar in these two states. The electron transfer reorganization energy for the charge separation (S2 to S1) and for charge recombination (S1 to S0) are expected to be similar.

II.2 DONOR-ACCEPTOR ELECTRONIC COUPLING CALCULATIONS

DA couplings were calculated using various methods, including fragment-based effective transfer integral method in ADF[7-9], block-diagonalization (BD) method and the orbital-based generalized Mulliken-Hush (GMH) methods[10-11]. The dipole moments and transition dipole moments of the associated ground and excited states in the orbital-based GMH calculations were approximated using the leading orbital configurations in the TD-DFT computations. More specifically, the DMA-G π orbital was used as the electron donor while the alkyne-anthracene π orbital was used as the electron acceptor. Within the energy range between the HOMO and HOMO-4, we select the occupied π orbital that has the largest combined amplitude on DMA and guanosine as the donor. Similarly, we select the π orbital with the largest combined amplitude on the alkyne group and anthracene as the acceptor. The GMH coupling is:

$$|H_{DA}| = \frac{|\vec{\mu}_{DA}||\Delta E|}{\sqrt{|\vec{\mu}_D - \vec{\mu}_A|^2 + 4|\vec{\mu}_{DA}|^2}} \tag{S1}$$

Here $\vec{\mu}_{DA}$ is the transition dipole moment between donor and acceptor orbitals, ΔE is the energy difference between donor and acceptor orbitals, $\vec{\mu}_D$ is the donor orbital dipole and $\vec{\mu}_A$ is the acceptor orbital dipole.

The GMH method generally performs well in two-state problems with weakly coupled donors and acceptors[10-12]. The DMA-GC-Anth has a coupling experimentally estimated to be less than $0.01eV$. Excited state analysis found that at the S2 equilibrium geometry (charge separation donor state), the energies of the S1 and S2 states are well separated from other states (> 0.6 eV), indicating a two-state system.

In BD calculations, the DMA-GC-Anth was divided into two fragments (donor fragment, DMA-G and acceptor fragment alkyne-anthracene) which are separated at the H-bonds between G and C. DFT analysis of the whole molecule generates the Kohn-Sham matrix F^{AO} in AO basis. The matrix is orthogonalized

$$H = (S^{AO})^{-\frac{1}{2}} \cdot F^{AO} \cdot (S^{AO})^{-\frac{1}{2}} \tag{S2}$$

before being divided into four blocks.

$$H = \begin{bmatrix} H_{DD} & H_{DA} \\ H_{AD} & H_{AA} \end{bmatrix} \tag{S3}$$

H_{DD} and H_{AA} were diagonalized using the matrices M_{DD} and M_{AA}. The eigenvectors of the blocks are MO's that are localized in each block. The molecular Hamiltonian H is:

$$H^{BD} = \begin{bmatrix} M_{DD} & 0 \\ 0 & M_{AA} \end{bmatrix}^{\dagger} \cdot \begin{bmatrix} H_{DD} & H_{DA} \\ H_{AD} & H_{AA} \end{bmatrix} \cdot \begin{bmatrix} M_{DD} & 0 \\ 0 & M_{AA} \end{bmatrix} \tag{S4}$$

The DA coupling is the off-diagonal element of H^{BD} that corresponds to the donor and acceptor orbitals. For charge separation, the donor (acceptor) orbital is a DMA-G π orbital (alkyne-anthracene π orbital). For charge recombination, the donor (acceptor) orbital is an alkyne-anthracene π^* orbital (DMA-G π orbital).

We also computed the DA coupling using the charge transfer integral method implemented in ADF. Following the same fragmentation scheme, the electronic structure of the fragments was calculated using the PBE functional with a TZ2P basis set. The coupling is

$$|H_{DA}| = \left| \frac{J_{DA} - \frac{S_{DA}(E_D + E_A)}{2}}{1 - S_{DA}^2} \right| \tag{S5}$$

J_{DA} is the charge transfer integral between donor and acceptor orbitals, S_{DA} is the overlap integral between donor and acceptor, E_D is the donor orbital energy and E_A is the acceptor orbital energy. This method does not rely on weak overlap assumptions, which are used in GMH. This approach is applicable to cases where molecular orbital of one molecule (fragment) couples to orbital from other molecules (fragments)[7]. The validity of these methods is examined further by comparing the computed couplings with those determined from experiments.

Temperature dependent kinetic data indicate donor-acceptor interaction[3] for charge separation is approximately 0.0066 eV. Table S3 shows that in the S2 equilibrium geometry, the GMH calculated coupling is ~0.008eV, the BD calculated coupling is also approximately 0.008eV, and ADF effective transfer integral method gives a coupling of ~0.013eV. Both the BD calculation and GMH calculation at the B3LYP/6-31G(d, p) level produce electronic couplings consistent with experiment. For charge recombination, the BD calculated coupling in the S1 equilibrium geometry is 0.0062eV.

Table S3. Comparison of calculated $|H_{DA}|$ for charge separation in DMA-GC-Anth using different methods in the S2 equilibrium geometry

Electronic Structure/Coupling Calculation Method	Calculated $|H_{DA}|$
B3LYP/6-31G(d, p)/GMH/ PCM solvent Model	0.00826eV
B3LYP/6-31G(d, p)/Block-Diagonalization	0.00729eV
B3LYP/6-31G(d, p)/block-diagonalization/PCM solvent Model	0.00795eV
PBE/6-31g(d, p)/block-diagonalization	0.00944eV
PBE/TZ2P/ transfer integral method in ADF	0.0126eV
Experiment	0.0066eV

II.3 INNER-SPHERE REORGANIZATION ENERGIES

Experimental studies found that the charge separation reaction free energy (ΔG) is $-0.41eV$ and the total reorganization energy is $\sim 1.0eV$ [3, 6]. Therefore, the activation free energy is $\sim 0.1eV$, a low barrier process. We calculate the inner-sphere reorganization energy for both charge separation and charge recombination using the "4-point" method.[13] With TD-B3LYP/6-31G(d,p) theory applied to the S1 and S2 equilibrium geometries, the computed inner-sphere reorganization energy for the charge separation process is 0.34eV. Using the S1 and S0 equilibrium structures, the computed inner sphere reorganization energy for charge recombination is 0.41eV. These two values, compared to the experimentally determined reorganization energies of ~1 eV, indicating that the outer-sphere reorganization energy dominates the total reorganization energy.

The composition of the ET reaction coordinate was analyzed by calculating the inner-sphere reorganization energy contribution from each vibrational mode for charge-separation and charge-recombination. We partition the guanosine and the DMA (the "donor fragment") together while the anthracene and cytidine are grouped together (the "acceptor fragment"). Both guanosine and cytidine were modified with a side chain (2', 3', 5'-tri-*O*-(*tert*-butyldimethylsilyl)ribofuranosidyl , Structure 1). To reduce the computational cost, we replaced the side chain on donor fragment with a $-SiH_3$ group. At the B3LYP/6-31G(d,p) level of theory, the neutral donor fragment with the original side chain has a dihedral angle of $\sim 45^o$ between the DMA and the guanosine planes. After replacing the original side chain with an $-SiH_3$ group, this dihedral angle was computed to be $\sim 32^o$, indicating this substitute reproduces the nature of the experimental system. As with the acceptor fragment, we replaced the side chain with an H atom, since the removal of side chain does not significantly change the dihedral angle between the anthracene and cytidine.

The contributions of inner-sphere reorganization energy from each vibrational mode of donor fragment and acceptor fragment are obtained by the means of DUSHIN code[14] in vacuum. The calculated donor fragment contribution of inner-sphere reorganization energy in charge-separation and charge-recombination are both ~ 1eV. It dominates the total inner-sphere reorganization energy as the acceptor contributes, based on DUSHIN calculations, 0.06 eV and 0.17 eV, respectively. Listed in Table S4 are the contributions of inner-sphere reorganization energy from each vibrational mode on acceptor fragment. They show that in both charge-separation and charge-recombination, the modes on acceptor fragment with frequency between 800 cm^{-1} and 1800 cm^{-1} contribute ~ 50% of all acceptor fragment inner-sphere reorganization energy. For charge-recombination, the acceptor modes with frequency between 800 cm^{-1} and 1800 cm^{-1} contribute only 6.5% of total inner-sphere reorganization energy (combining contributions from both fragments). Hence the compositions of inner-sphere reorganization energy for charge-separation and those for charge-recombination are similar.

Table S4. Decomposition of inner-sphere reorganization energy contributed by acceptor fragment computed for both charge-separation and charge-recombination.

	Charge-separation		Charge-recombination	
Mode #	Frequency / cm^{-1}	λ_i contribution / %	Frequency / cm^{-1}	λ_i contribution / %
7	26	0.34	18	1.66
8	29	0.08	26	0.57
9	34	0.30	29	0.92
10	69	2.23	73	0.01
11	88	0.02	86	0.01
12	105	2.89	107	0.58
13	115	0.00	120	0.00
14	155	0.40	165	0.03
15	171	3.53	173	0.60
16	202	0.11	204	0.04
17	243	0.11	238	0.01
18	264	2.66	266	0.40

19	283	8.39	285	0.26
20	320	0.32	341	0.72
21	363	0.06	354	0.58
22	368	1.76	370	0.28
23	378	1.38	386	0.38
24	386	0.00	397	0.16
25	395	0.23	402	12.05
26	413	0.02	425	0.06
27	434	1.19	436	0.86
28	458	0.15	484	1.23
29	467	0.47	487	0.00
30	490	0.66	495	0.35
31	518	0.04	506	0.01
32	520	0.04	525	3.34
33	532	0.23	549	0.09
34	547	0.21	569	0.00
35	589	0.28	582	0.65
36	594	0.13	596	0.20
37	607	0.02	619	0.38
38	616	0.32	636	0.01
39	633	0.02	640	0.01
40	641	3.27	643	0.01
41	652	0.32	656	2.53
42	684	0.00	685	4.97
43	723	0.00	737	0.47
44	732	0.06	746	5.85
45	737	0.06	755	0.03
46	741	1.32	758	0.01
47	745	0.00	769	0.01
48	747	0.00	778	0.26
49	764	0.02	781	4.02
50	775	0.13	801	0.00
51	829	0.00	867	0.01
52	853	0.02	877	0.00
53	876	1.27	881	0.00
54	884	0.06	884	0.14
55	889	0.00	906	0.00
56	906	0.02	918	1.58
57	910	1.30	926	0.06

58	913	0.40	943	0.01
59	916	0.68	968	0.00
60	937	0.00	974	0.02
61	955	0.00	997	0.00
62	956	0.00	1003	0.01
63	1059	1.42	1046	0.52
64	1064	1.00	1048	0.19
65	1069	0.00	1054	0.01
66	1089	2.17	1095	0.64
67	1112	0.00	1136	0.01
68	1153	0.00	1177	0.05
69	1181	0.00	1180	0.56
70	1187	1.95	1194	0.02
71	1194	2.91	1200	5.33
72	1219	0.02	1211	0.01
73	1233	7.65	1242	4.03
74	1280	0.13	1262	0.00
75	1285	1.04	1295	6.56
76	1307	0.06	1302	0.04
77	1308	0.11	1320	0.46
78	1317	0.32	1339	0.42
79	1346	0.00	1358	0.00
80	1395	0.02	1413	5.51
81	1404	14.36	1423	0.00
82	1433	0.11	1425	0.01
83	1439	0.00	1444	0.38
84	1459	0.34	1468	1.98
85	1471	0.00	1488	0.03
86	1485	0.57	1490	0.58
87	1489	2.89	1494	0.50
88	1537	4.84	1531	0.94
89	1546	0.08	1567	0.89
90	1556	0.49	1574	0.01
91	1580	0.00	1608	7.80
92	1588	0.04	1626	0.00
93	1596	3.42	1633	0.45
94	1626	4.52	1674	0.01
95	1630	2.40	1685	0.13
96	1691	2.34	1710	2.31

97	1805	3.95	1823	2.18
98	2221	1.32	2295	4.41
99	3173	0.00	3179	0.00
100	3184	0.00	3184	0.00
101	3185	0.04	3185	0.00
102	3192	0.00	3193	0.01
103	3193	0.02	3194	0.01
104	3204	0.00	3207	0.02
105	3205	0.06	3207	0.06
106	3214	0.00	3216	0.01
107	3215	0.79	3217	0.00
108	3231	0.11	3227	2.00
109	3596	0.21	3602	0.18
110	3625	0.40	3634	3.60
111	3734	0.36	3739	0.69

III. THEORY OF IR PERTURBED NON-ADIABATIC ET

Fermi's golden rule (FGR) provides the starting point to describe ET in weakly coupled donor-bridge-acceptor (DBA) structures. Writing FGR in the time domain allows analytics of IR effects in the context of electronic coupling fluctuations and donor-acceptor energy gap fluctuations (Figure S3).[15-17] Vibrational excitation of the modes driving energy gap fluctuations and the modes driving donor-acceptor coupling fluctuations are possible, and these modes can also be populated by intramolecular vibrational energy redistribution (IVR). For simplicity, each vibrational mode in our modeling is assumed to be either modulating donor-acceptor (DA) couplings or DA energy gap, but not both.

$$k_{ET} = \frac{2\pi}{\hbar}\sum_{\nu}\sum_{a} P_\nu P_a \sum_{\mu}\sum_{b}\left|\langle D,\nu,a|\hat{H}|A,\mu,b\rangle\right|^2 \delta\left(E_{D,\nu,a} - E_{A,\mu,b}\right) \tag{4}$$

$$= \frac{1}{\hbar^2}\int_{-\infty}^{+\infty} e^{-\frac{it}{\hbar}\Delta G}\, dt \left[\sum_{\nu}\sum_{\mu} P_\nu\, S_{\nu\mu} e^{\frac{i}{\hbar}(E_\nu - E_\mu)t}\right]\left[\sum_{a} P_a \langle a|\hat{H}_{DA}(t)\hat{H}_{DA}(0)|a\rangle\right] \tag{5}$$

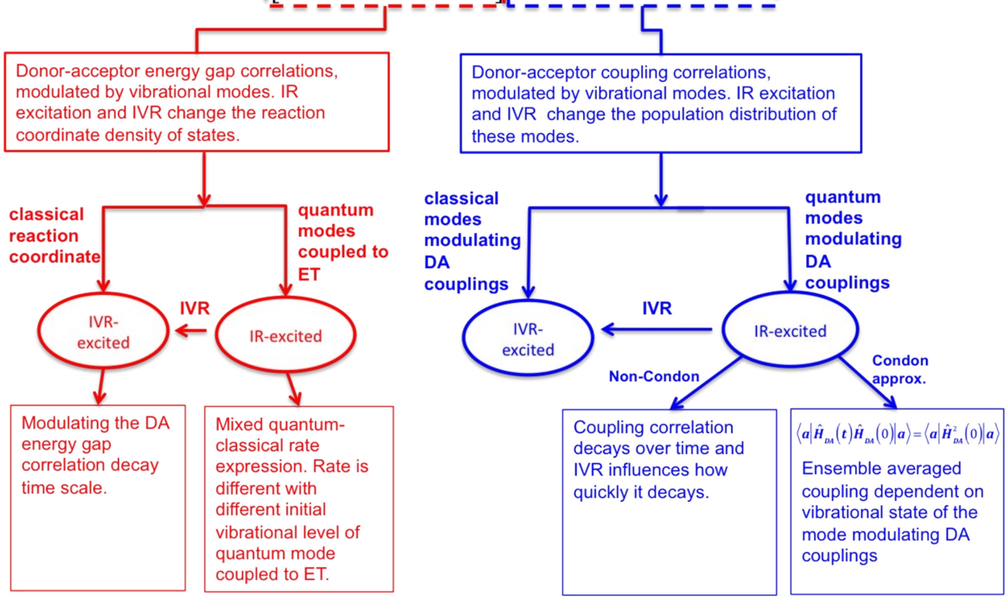

Figure. S3. A roadmap to IR-induced ET rate modulation mechanisms. IR modulation can arise from the excitation of modes that modulation DA energy gap (left side, red routes) or the modes that influence the DA electronic couplings (right side, blue routes). IR excitation can excite high-frequency quantum modes ($\hbar\omega \gg k_BT$), and IVR can populate classical modes ($\hbar\omega < k_BT$). The effect of IR excitation on the rate depends on the time scales of ET dynamics and of vibrational motion. Characteristic time scales at play are the ET reaction time (k_{ET}^{-1}), the donor-acceptor energy gap fluctuation time (τ_{FC}), the coupling fluctuation time (τ_c), and the IVR time (τ_{IVR}).

The indices ν and μ in Eq. S6 denote the mode modulating DA energy gap, while a and b denote the modes modulating DA couplings, respectively. $|\nu\rangle$ and $|a\rangle$ denote the vibrational wavefunctions of the two types of modes, respectively. $\hat{H}$ is the electronic Hamiltonian. P_ν and P_a are the initial populations of these two types modes, respectively. $S_{\nu\mu} = |\langle\nu|\mu\rangle|^2$ is the Franck-Condon overlap of the energy gap modulating mode. $E_{D,\nu,a}$ and $E_{A,\mu,b}$ are the initial and final vibronic state energies, respectively. $\hat{H}_{DA}(t)$ is the time-dependent DA coupling. IR excitation and subsequent IVR produce non-equilibrium population distribution for both the modes modulating DA couplings and the modes modulating DA energy gap. This time domain framework allows us to dissect the influence of IR excitation on ET systems.

Non-adiabatic ET rate may also be written in the time domain[17-18] using Eq. S8.

$$k_{ET} = \frac{1}{\hbar^2}\int e^{-\frac{it}{\hbar}\Delta G} dt \left[\sum_{v} P_v \langle \Delta U_v(t)\Delta U_v(0)\rangle\right]\left[\sum_{a} P_a \langle a \,|\, \hat{H}_{DA}(t)\hat{H}_{DA}(0) \,|\, a\rangle\right] \tag{S8}$$

ΔG is the ET reaction free energy. $\langle \Delta U_v(t)\Delta U_v(0)\rangle$ is the DA energy gap correlation function contributed by population on the vibrational level v of energy gap modulating mode. $\langle a \,|\, \hat{H}_{DA}(t)\hat{H}_{DA}(0) \,|\, a\rangle$ is the DA coupling correlation function contributed by the populations on the vibrational level a of the coupling modulating mode.

III.1 NON-CONDON EFFECTS

IR excitation and subsequent IVR can accelerate the DA coupling fluctuation (shortens the DA coupling fluctuation time scale τ_c). When τ_c is shorter than the DA energy gap fluctuation time τ_{FC}, Condon approximation fails. Therefore, IR-excitation and subsequent IVR can invalidate the Condon approximation and influence the ET rate. The IR-induced non-Condon effect and its influence on ET rate is described by Troisi et al.[18] Following Troisi et al., the predicted magnitudes of IR-induced charge-recombination rate increase of DMA-GC-Anth are listed in Table S5.

The IR-induced ET rate modulation via non-Condon effect is analogous to a two-level (donor and acceptor) system with time-dependent coupling between donor and acceptor levels (e.g. created by external fields). If the oscillating frequency of the time-dependent coupling is resonant with the donor-acceptor energy gap, the transition probability from donor level to acceptor level reaches maximum. In general, time-dependent coupling may have components that oscillate at low frequencies (static components) and also components that are highly oscillatory. IR-excitation is expected to produce more highly oscillating components and effectively reduce the magnitude of static components of time-dependent coupling. Therefore, if donor-acceptor energy gap is small (near activationless ET), IR-excitation reduces static coupling components magnitude and slows the ET rate. If donor-acceptor energy gap is large (highly activated ET), IR excitation accelerates ET rate by increasing the magnitude of highly oscillating coupling components.

Table S5. Predicted ratio of $k_{ET}(\tau_c^{IR})/k_{ET}(\tau_c = 25fs)$ with different values of $\langle H_{DA}\rangle^2/\langle H_{DA}^2\rangle$ and τ_c^{IR} for the charge-recombination in DMA-GC-Anth. The reaction free energy ΔG is -2.5 eV and total reorganization energy λ is 1 eV.

$\langle H_{DA}\rangle^2/\langle H_{DA}^2\rangle$	τ_c^{IR} / fs		
	5	10	20
	$k_{ET}(\tau_c^{IR})/k_{ET}(\tau_c = 25fs)$		
1.00	1.0	1.0	1.0
0.90	1.7	1.2	1.0
0.50	4.3	1.7	1.1
0.10	6.3	2.2	1.1
0.00	6.8	2.3	1.4

III.2 IR-INDUCED RATE MODULATION UNDER CONDON APPROXIMATION

When DA coupling fluctuations are substantially slower than the Franck-Condon time ($\tau_c > \tau_{FC}$), the Condon approximation holds and the mean squared DA coupling enters the rate[17-18]:

$$k_{ET} = \frac{1}{\hbar^2}\langle H_{DA}^2\rangle \sum_{\nu} P_{\nu} \sum_{\mu} \int |\langle \nu|\mu\rangle|^2 \exp\left[\frac{it}{\hbar}\left(E_{\nu} - E_{\mu} - \Delta G\right)\right] dt \tag{S9}$$

Listed in Tables S6 and S7 are the computed percentage change of mean squared DA couplings caused by the excitation of vibrational modes in DMA-GC-Anth. These modes include the IR-excited H-bond modes and IVR-excited H-bond out-of-plane modes. We also examined the quantum modes in the frequency range of 1300 – 1500 cm^{-1} as they can be IVR excited. The DA couplings are calculated using block-diagonalization and generalized Mulliken-Hush methods (see Section II in this SI).

Table S6. IR-excited in-plane H-bond modes and IVR-excited out-of-plane H-bond modes of DMA-GC-Anth and the percentage differences between the expected values of $\langle H_{DA}^2 \rangle$ calculated at vibrational level 1 and those calculated at vibrational level 0. Couplings are calculated using block-diagonalization method and GMH method.

Mode No.	Vibrational frequency/cm^{-1}	Percentage difference of couplings computed with block-diagonalization method		Percentage difference of couplings computed with GMH method	
		CS	CR	CS	CR
524	1526.64	-7.13	-8.30	-6.80	-7.23
541	1542.55	-7.80	-7.46	-8.00	-9.22
543	1545.34	-6.53	-7.02	-6.71	-6.27
544	1565.97	-6.48	-6.95	-6.30	-6.90
547	1604.22	-6.74	-6.34	-6.40	-7.66
551	1655.61	-4.43	-2.44	-3.15	-4.40
552	1664.51	-4.55	-3.72	-4.54	0.73
553	1669.95	-5.82	-5.76	-5.52	-2.97
556	1690.43	-4.81	-5.61	-4.39	-5.15
557	1700.64	-3.58	-1.88	-3.77	-3.39
559	1746.26	-3.91	-3.51	-2.89	2.20
188	514.19	-3.86	-4.69	-3.84	-4.07
190	528.76	-3.96	-4.44	-3.93	-4.24
209	647.48	2.08	7.77	1.91	4.03
210	649.85	-0.44	1.38	-0.35	-0.26
215	671.83	-0.77	-0.22	-0.62	-1.29
222	700.19	0.22	2.07	0.09	0.97
223	702.88	-0.79	-0.25	-0.90	-0.05
224	717.70	-0.78	-0.41	-0.79	-0.64
225	726.82	0.00	0.47	-0.07	0.35

226	729.30	-1.20	-1.63	-1.32	-0.75
228	752.04	-0.50	0.14	-0.54	-0.21
232	768.29	-0.22	-1.03	-0.38	0.25
233	771.16	-0.24	0.99	-0.40	0.41
236	783.70	-0.28	-1.20	-0.21	-0.60
245	824.65	0.41	-3.13	0.54	-0.08
246	825.00	2.80	-9.99	3.22	1.38
262	914.64	0.88	-1.96	0.46	-0.38
264	921.45	0.14	0.44	0.04	0.87

Table S7. List of IVR modes of DMA-GC-Anth molecule and the percentage differences between the expected values of $\langle H_{DA}^{2} \rangle$ calculated at vibrational level 1 and those calculated at vibrational level 0. Couplings are calculated using block-diagonalization method and GMH method.

Mode No.	Vibrational frequency/cm^{-1}	Percentage difference of couplings computed with block-diagonalization method		Percentage difference of couplings computed with GMH method	
		CS	CR	CS	CR
400	1292.09	-3.98	-4.00	-4.03	-3.83
401	1292.20	-3.97	-3.86	-4.00	-3.78
402	1294.53	-3.88	-3.86	-3.87	-3.72
403	1295.42	-4.06	-4.41	-4.05	-4.08
404	1299.18	-4.06	-3.80	-2.96	-0.46
405	1300.98	-3.84	-3.81	-3.68	-3.46
406	1302.82	-3.94	-3.88	-3.98	-3.76
407	1311.83	-3.89	-4.20	-3.70	-3.40
408	1313.56	-3.73	-3.46	-3.85	-3.15
409	1316.85	-3.84	-2.76	-3.25	-0.55
410	1318.17	-3.98	-4.18	-3.84	-4.42
411	1327.95	-3.41	-3.27	-3.36	-3.02
412	1336.30	-3.20	-2.70	-3.30	-2.71
413	1338.05	-3.49	-3.43	-3.56	-3.35
414	1338.30	-3.45	-3.25	-3.30	-3.24
415	1357.54	-3.02	-4.71	-2.02	-5.82
416	1358.14	-3.42	-4.13	-3.18	-4.36
417	1365.64	-3.33	-3.46	-3.26	-3.55
418	1371.70	-3.06	-2.31	-3.05	-3.15
419	1372.11	-3.61	-3.55	-3.54	-2.60
420	1373.12	-3.46	-3.18	-3.41	-2.22
422	1386.74	-3.37	-3.17	-3.34	-2.73

423	1390.15	-3.21	-2.45	-3.01	0.53
424	1392.12	-3.32	-3.15	-3.36	-3.04
425	1395.59	-2.81	-2.58	-2.52	1.98
426	1396.11	-3.03	-3.18	-2.87	-3.18
427	1399.26	-3.03	-2.91	-3.06	-3.10
428	1401.63	-2.81	-2.77	-2.71	-3.07
429	1402.60	-3.02	-2.91	-3.03	-3.04
430	1402.76	-2.98	-2.87	-2.97	-2.95
431	1403.25	-3.11	-3.19	-3.17	-2.93
432	1404.62	-3.01	-3.02	-2.94	-3.21
433	1405.76	-2.91	-2.84	-2.88	-3.04
434	1406.56	-3.03	-2.97	-3.08	-2.87
435	1406.84	-3.01	-3.12	-3.10	-2.91
436	1407.80	-2.96	-3.34	-2.93	-3.10
437	1408.24	-2.99	-3.11	-2.91	-3.16
438	1408.73	-2.92	-2.74	-2.86	-2.94
439	1409.81	-2.89	-2.74	-2.96	-2.79
440	1411.10	-2.97	-3.18	-2.97	-3.14
441	1413.78	-2.82	-3.05	-2.74	-3.00
442	1414.06	-2.86	-3.21	-2.69	-2.81
443	1416.02	-2.87	-2.90	-2.90	-2.90
444	1417.45	-2.93	-3.07	-2.95	-2.92
445	1417.46	-2.89	-3.09	-2.85	-3.00
446	1419.10	-2.36	-3.20	-1.97	-2.49
447	1420.16	-2.95	-2.98	-2.91	-3.16
448	1421.80	-2.76	-3.19	-2.64	-3.27
449	1423.35	-2.74	-2.56	-2.70	-2.67
450	1423.57	-3.01	-2.20	-3.27	-1.97
451	1424.60	-2.92	-3.24	-2.82	-3.26
452	1427.49	-2.81	-3.01	-2.74	-2.76
453	1429.84	-2.57	-2.21	-2.60	-2.33
454	1430.48	-2.81	-2.93	-2.86	-2.70
455	1431.09	-2.74	-2.42	-2.74	-2.64
456	1438.14	-2.75	-3.07	-2.71	-2.93
457	1439.19	-2.70	-2.88	-2.53	-2.24
458	1440.97	-2.69	-2.64	-2.70	-2.64
459	1441.02	-2.53	-2.13	-2.60	-2.21
460	1441.57	-2.71	-2.64	-2.71	-2.62
461	1442.49	-2.72	-2.78	-2.65	-2.55
462	1443.48	-2.60	-2.64	-2.61	-2.66
463	1446.06	-2.64	-2.63	-2.61	-2.86
464	1447.15	-2.48	-2.29	-2.41	-2.31
465	1447.84	-2.61	-2.35	-2.57	-2.78
466	1453.98	-2.31	-2.15	-2.50	-1.47
467	1458.66	-2.54	-2.37	-2.56	-2.45
468	1465.39	-2.36	-0.56	-1.49	-1.20
469	1473.07	-2.00	-2.32	-1.87	-1.62

470	1476.10	-2.53	-2.98	-2.19	-3.08
471	1484.14	-2.40	-2.15	-2.49	-2.10
472	1484.72	-2.42	-2.38	-2.42	-2.38
473	1484.83	-2.39	-2.31	-2.40	-2.26
474	1486.17	-2.35	-2.43	-2.38	-2.46
475	1486.71	-2.30	-2.25	-2.33	-2.09
476	1488.53	-2.21	-1.98	-2.28	-1.93
477	1489.11	-2.44	-2.53	-2.51	-2.30
478	1491.45	-2.51	-2.49	-2.51	-2.19
479	1491.59	-2.26	-2.14	-2.29	-2.45
480	1492.81	-2.35	-2.02	-2.33	-1.35
481	1493.42	-2.28	-2.07	-2.29	-2.20
482	1493.55	-2.32	-2.28	-2.31	-2.31
483	1494.06	-2.20	-2.41	-2.18	-2.16
484	1494.46	-2.24	-2.23	-2.22	-2.25
485	1495.56	-2.32	-2.60	-1.68	1.17
486	1496.04	-2.14	-2.07	-2.03	-1.65
487	1496.40	-2.29	-2.37	-2.29	-1.06
488	1496.63	-2.31	-1.98	-2.31	-2.17
489	1496.69	-2.14	-2.05	-2.11	-2.16
490	1497.58	-2.32	-2.22	-2.35	-2.20
491	1497.77	-2.29	-2.26	-2.32	-2.09
492	1498.47	-2.27	-2.23	-2.23	-2.32
493	1499.57	-2.28	-2.26	-2.32	-2.15
494	1500.39	-2.16	-1.99	-2.11	-2.08
495	1500.56	-2.23	-2.03	-2.27	-2.02
496	1501.74	-2.28	-2.04	-2.26	-2.38
497	1502.03	-2.26	-2.29	-2.25	-2.14
498	1504.03	-2.14	-2.41	-2.05	-2.32
499	1505.78	-2.28	-2.07	-2.25	-2.36
500	1506.57	-2.32	-2.25	-2.35	-2.21
501	1506.62	-2.16	-2.27	-2.21	-1.98
502	1507.35	-2.29	-2.22	-2.34	-2.04
503	1508.23	-2.28	-2.22	-2.34	-2.12
504	1508.57	-2.23	-1.97	-2.21	-2.08
505	1508.75	-2.10	-2.41	-2.07	-2.29
506	1509.58	-2.09	-1.53	-2.15	-1.70
507	1509.86	-2.25	-2.24	-2.30	-2.16
508	1510.20	-2.02	-1.79	-2.02	-1.90
509	1510.49	-2.11	-1.85	-2.28	-1.73
510	1511.46	-2.20	-1.76	-2.32	-1.79
511	1512.04	-2.34	-2.26	-2.40	-2.07
512	1514.23	-2.20	-2.35	-2.17	-2.10
513	1516.04	-2.26	-2.23	-2.27	-2.33
514	1516.76	-2.05	-2.08	-2.06	-1.86
515	1517.80	-2.21	-2.18	-2.27	-2.03
516	1518.98	-2.21	-2.00	-2.26	-2.07

517	1519.06	-2.23	-2.30	-2.22	-2.28
518	1519.46	-2.13	-2.29	-2.10	-2.25
519	1519.46	-2.47	-2.51	-2.25	-2.99
520	1520.73	-2.15	-2.34	-2.13	-2.26
521	1522.78	-2.09	-2.00	-2.13	-1.94
522	1523.24	-2.18	-2.60	-2.17	-2.31
523	1524.06	-2.07	-2.03	-2.07	-2.19
525	1526.83	-2.07	-2.46	-2.09	-1.97
526	1527.45	-2.12	-2.33	-2.05	-2.47
527	1528.08	-2.17	-2.68	-2.17	-2.22
528	1528.94	-2.23	-2.66	-2.23	-2.06
529	1529.52	-2.25	-1.91	-2.00	-0.02
530	1530.14	-2.19	-2.27	-2.16	-2.34
531	1531.12	-2.04	-2.01	-2.05	-1.87
532	1532.22	-2.05	-2.14	-2.11	-1.80
533	1532.70	-1.92	-1.99	-1.93	-1.88
534	1534.18	-2.23	-2.01	-2.04	-2.65
535	1534.55	-1.90	-2.41	-1.78	-2.30
536	1534.91	-2.12	-2.38	-2.13	-1.94
537	1536.04	-1.92	-1.95	-1.99	-1.75
538	1536.47	-2.16	-2.13	-2.25	-1.92
539	1537.35	-2.01	-1.73	-2.11	-1.64
540	1539.71	-1.99	-2.36	-1.95	-2.15

III.3. IR INDUCED CHANGES TO THE QUANTUM FRANCK-CONDON FACTOR

For ET with mixed quantum-classical reaction coordinate, ET rate is described by semi-classical rate expression[19] (see Eqns. 5 and 6 in main text). The Franck-Condon summation factor in semi-classical rate expression with the quantum reaction coordinate initially at vibrational ground state ($FC_{\nu=0}$) is different from that with the quantum mode initially populated on vibrational level 1 ($FC_{\nu=1}$).

Figures S4(a)-(i) show $\log_{10}\left(\frac{FC_{\nu=0}}{FC_{\nu=1}}\right)$ as a function of λ_i ($\lambda_i = S\hbar\omega$, the inner-sphere reorganization energy contributed by the quantum mode), λ_o (the classical component of total reorganization energy), and the driving force ΔG. We varied the value of λ_i between 0 and $2eV$, and ΔG between $0.5eV$ and $-1.5eV$. The

$FC_{v=0}$ and $FC_{v=1}$ factors were calculated with $\hbar\omega = 1{,}700cm^{-1}, 1{,}000cm^{-1}, 500cm^{-1}$. The values used for λ_o were 0.2 eV, 0.4 eV and 0.6 eV. For most parameter values IR excitation enhances the ET. However, a narrow parameter region causes the Franck-Condon summation factor to become smaller as a result of IR excitation. Figs. S4(a)-(i) indicate that the most significant IR-reducing-ET effect with a mixed classical-quantum reaction coordinate occurs when parameters satisfy $\Delta G + \lambda_o + \lambda_i - \hbar\omega \approx 0$. Here, the value of μ in the Franck-Condon overlap as a function of final vibrational state μ in semi-classical ET rate expression (Eq. 5a, main text) peaks roughly at the same value of μ as the exponential factor ($\exp\left[-\frac{(\Delta G + \mu\hbar\omega + \lambda_o)^2}{4\lambda_o kT}\right]$ in $FC_{v=0}$) peaks.

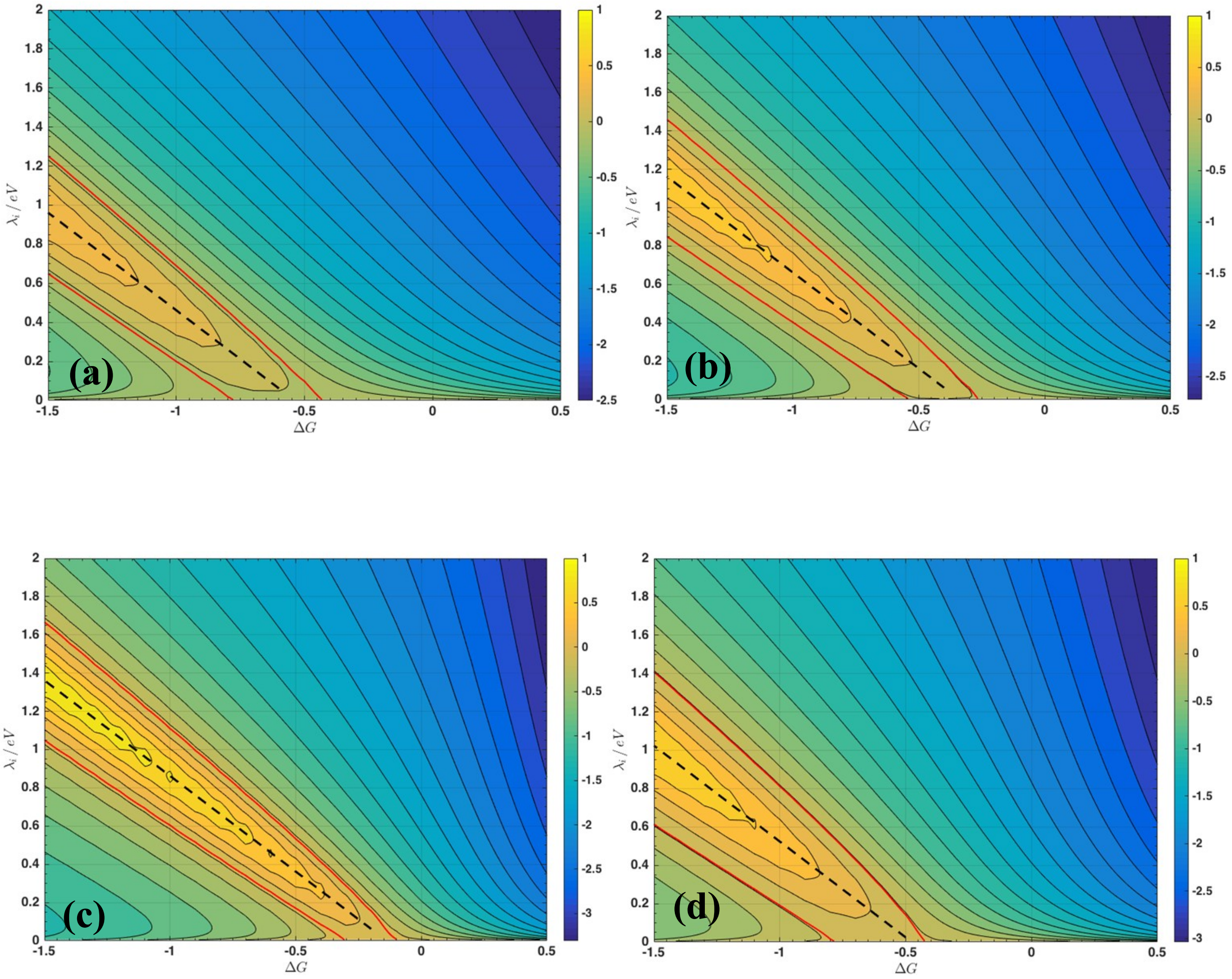

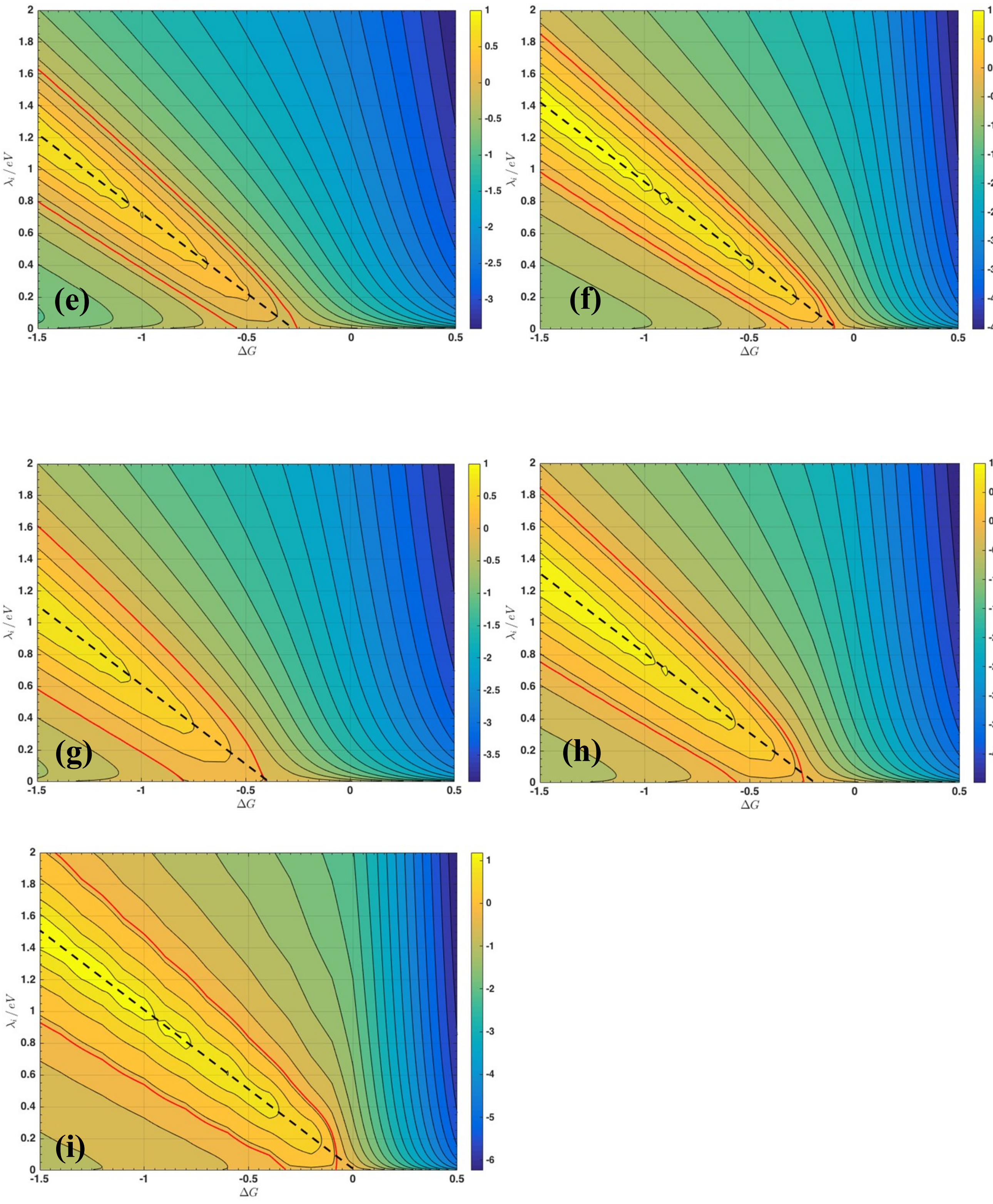

Figure. S4. Computed $\log_{10}\left(\frac{FC_{\nu=0}}{FC_{\nu=1}}\right)$ as a function of λ_i, λ_o and the driving force ΔG. The red solid lines indicate $\frac{FC_{\nu=0}}{FC_{\nu=1}}=1$ and the black dash lines indicate $\Delta G+\lambda_i+\lambda_o-\hbar\omega=0$. For each plot, the band between the red solid lines is the region where IR-excitation of the quantum mode that contributes to reaction coordinate reduces ET rate. The values of λ_o and vibrational frequency ($\hbar\omega$) used for each plot are: (a) $\lambda_o = 0.6\ eV$, $\hbar\omega = 500\ cm^{-1}$; (b) $\lambda_o = 0.4\ eV$, $\hbar\omega = 500\ cm^{-1}$; (c) $\lambda_o = 0.2\ eV$, $\hbar\omega = 500\ cm^{-1}$; (d) $\lambda_o = 0.6\ eV$, $\hbar\omega = 1000\ cm^{-1}$; (e) $\lambda_o = 0.4\ eV$, $\hbar\omega = 1000\ cm^{-1}$; (f) $\lambda_o = 0.2\ eV$, $\hbar\omega = 1000\ cm^{-1}$; (g) $\lambda_o = 0.6\ eV$, $\hbar\omega = 1700\ cm^{-1}$; (h) $\lambda_o = 0.4\ eV$, $\hbar\omega = 1700\ cm^{-1}$; (i) $\lambda_o = 0.2\ eV$, $\hbar\omega = 1700\ cm^{-1}$.

Both $FC_{\nu=0}$ and $FC_{\nu=1}$ are summation series (see Eqns. 5 and 6 in main text). Each term in the sum of $FC_{\nu=0}$ and $FC_{\nu=1}$ has two component, quantum Franck-Condon overlap factor $P(\mu)$ and exponential factor $R(\mu)$. $P_{\nu=0}(\mu) = e^{-S}S^{\mu}/\mu!$ and $P_{\nu=1}(\mu) = e^{-S}S^{\mu-1}(\mu - S)^2/\mu!$. $R_{\nu=0}(\mu) = \exp\left[-\frac{(\Delta G + \mu\hbar\omega + \lambda_o)^2}{4\lambda_o kT}\right]$ and $R_{\nu=1}(\mu) = \exp\left[-\frac{(\Delta G + (\mu-1)\hbar\omega + \lambda_o)^2}{4\lambda_o kT}\right]$. Figs. S5(a) and S5(b) show the values of $P(\mu)$ and $R(\mu)$ as a functions of ET final vibrational state μ of the quantum mode contributing to reaction coordinate with $\Delta G = -1.0eV$, $\lambda_o = 0.60eV$, $\lambda_i = 0.525eV$ and $\hbar\omega = 1000cm^{-1}$. These parameters satisfy $\Delta G + \lambda_o + \lambda_i - \hbar\omega \approx 0$. The quantum Franck-Condon factor with $\nu = 0$ ($P_{\nu=0}(\mu)$) peaks at $\mu = 3$ while $P_{\nu=1}(\mu)$ has two peaks at $\mu = 2$ and $\mu = 7$. At low μ ($\mu \leq 2$), $P_{\nu=1} > P_{\nu=0}$ while $R_{\nu=1} < R_{\nu=0}$. $FC_{\nu=0}$ and $FC_{\nu=1}$ values are similar when $\mu \leq 2$. For $\mu = 3 - 5$, both $P_{\nu=0}$ and $R_{\nu=0}$ peak while $P_{\nu=1}$ reaches a minimum between these peaks. This difference in the quantum Franck-Condon factor causes the $FC_{\nu=0}$ factor to become significantly larger than the $FC_{\nu=1}$ factor as shown in Figs. S5(c) and S5(d). The IR effect is to move the system away from the activationless regime.

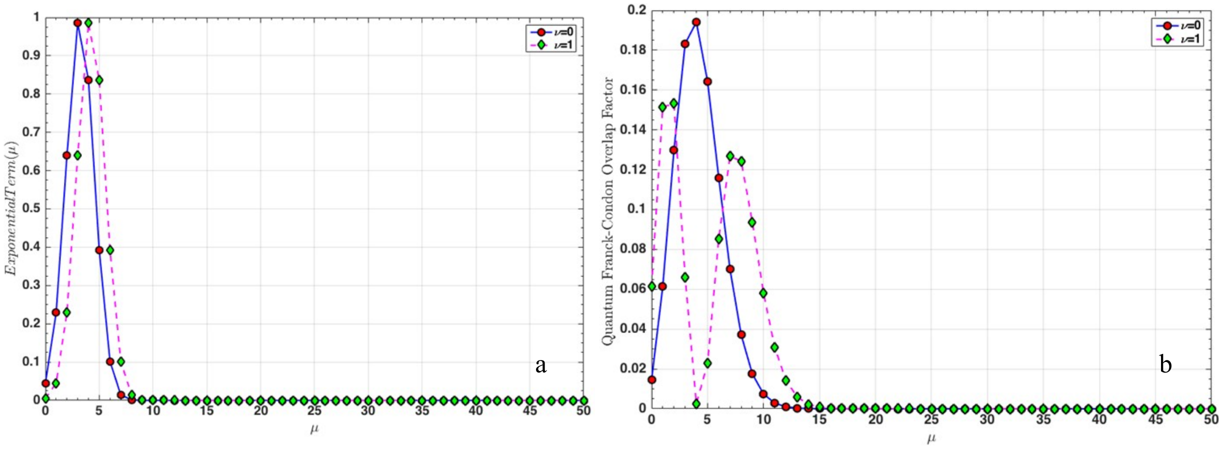

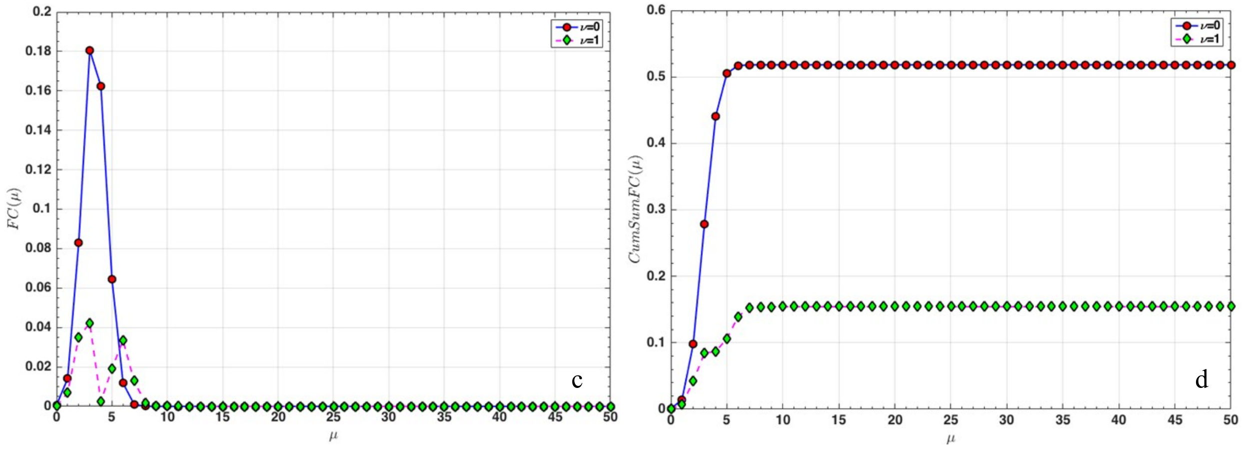

Figure S5. Plot of (a) exponential factors, (b) quantum Franck-Condon overlap factor, (c) Franck-Condon summation factors scaled by $\sqrt{4\lambda_o k_B T}$, and the (d) cumulative sum of terms in the scaled Franck-Condon summation as functions of finial vibrational level μ. Parameters used are: $\lambda_o = 0.60eV$, $\Delta G = -1.0eV$, $\lambda_i = 0.525eV$ and $\hbar\omega = 1000cm^{-1}$.

When ΔG is large and positive or λ_i is large ($\Delta G + \lambda_i + \lambda_o \gg \hbar\omega$), IR excitation strongly enhances ET (upper right corner Fig. S4). Fig. S6 shows the quantum Franck-Condon factors, exponential factors, $FC_{\nu=0}$, and $FC_{\nu=1}$ calculated with $\Delta G = -0.10eV$, $\lambda_i = 1eV$, $\lambda_o = 0.60eV$ and $\hbar\omega = 1000cm^{-1}$. $R_{\nu=1}$ is always larger than $R_{\nu=0}$ for all μ values (see Eq. 5(b) and Eq. 6 in main text). For more positive ΔG values, this comparison holds. When $\mu \leq 4$, $P_{\nu=1}$ is also larger than $P_{\nu=0}$, causing a rapid increase in $FC_{\nu=1}$ (Figs. S6(c) and S6(d)). For $\mu \geq 4$, although $P_{\nu=0}$ reaches its peak at μ~8, the value of $R_{\nu=0}$ is small. Therefore, these $P_{\nu=0}(\mu)R_{\nu=0}(\mu)$ do not significantly contribute to $FC_{\nu=0}$. As a result, $FC_{\nu=1} > FC_{\nu=0}$ and IR enhances ET reaction.

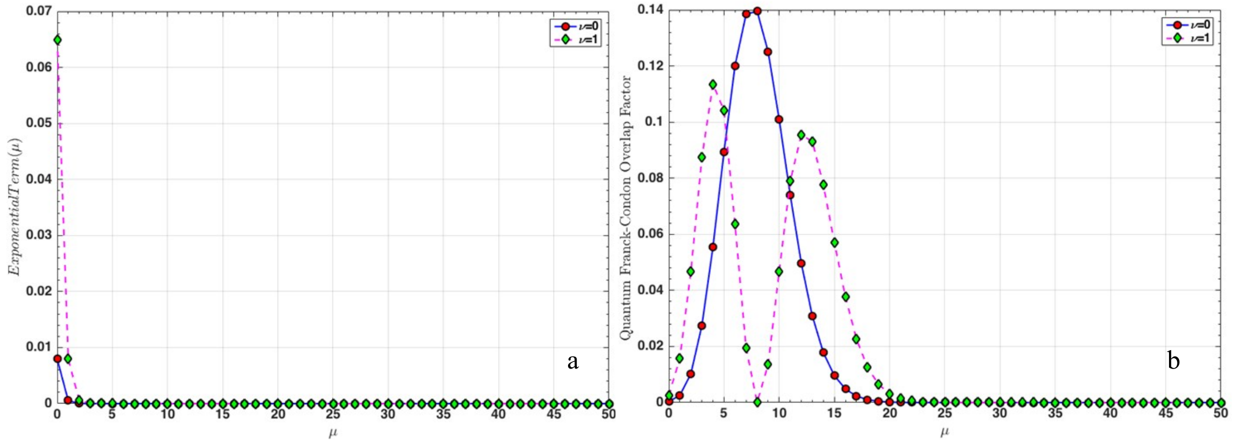

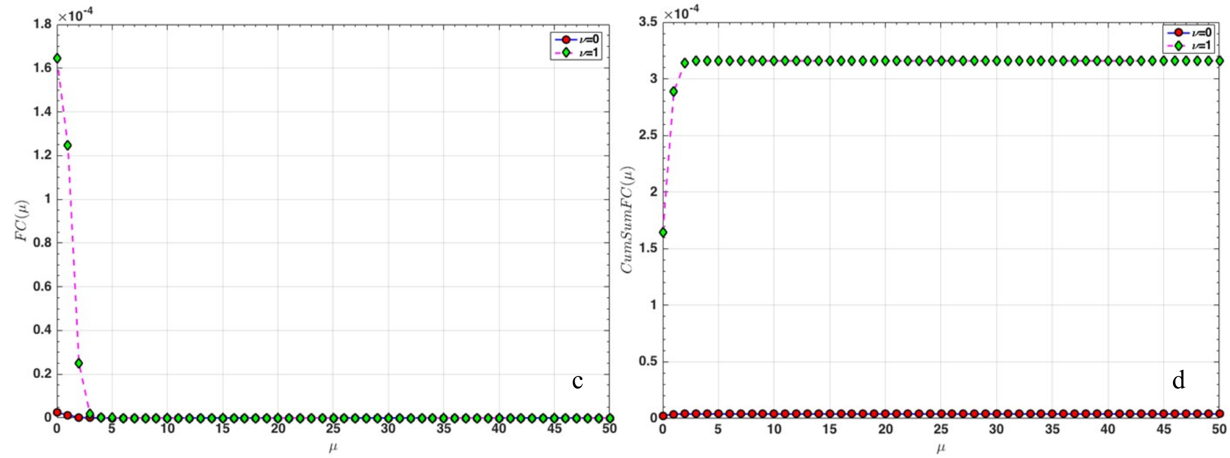

Figure S6. Plot of (a) exponential factors, (b) quantum Franck-Condon overlap factor, (c) Franck-Condon summation factors scaled by $\sqrt{4\lambda_o k_B T}$, and the (d) cumulative sum of terms in the scaled Franck-Condon summation as functions of finial vibrational level μ. Parameters used are: $\lambda_o = 0.60eV$, $\Delta G = -0.1eV$, $\lambda_i = 1.0eV$ and $\hbar\omega = 1000cm^{-1}$.

Another mixed classical-quantum ET regime is indicated at the bottom left corner of Fig. S4, where ΔG is negative or λ_i is small ($\Delta G + \lambda_i + \lambda_o \ll \hbar\omega$). In this regime, the peaks of both $R_{\nu=0}$ and $R_{\nu=1}$ occur at relatively large μ values, and the ratio between the quantum Franck-Condon factors $P_{\nu=1}/P_{\nu=0} = (\mu - S)^2/S$ is always larger than 1 when μ is large. Therefore, a larger $FC_{\nu=1}$ factor results. Fig. S7 shows the quantum Franck-Condon factors, exponential factors, $FC_{\nu=0}$, and $FC_{\nu=1}$ for $\Delta G = -1.40eV$, $\lambda_i = 0.1eV$, $\lambda_o = 0.60eV$ and $\hbar\omega = 1000cm^{-1}$. The contributions to the ET rate from small μ values are negligible.

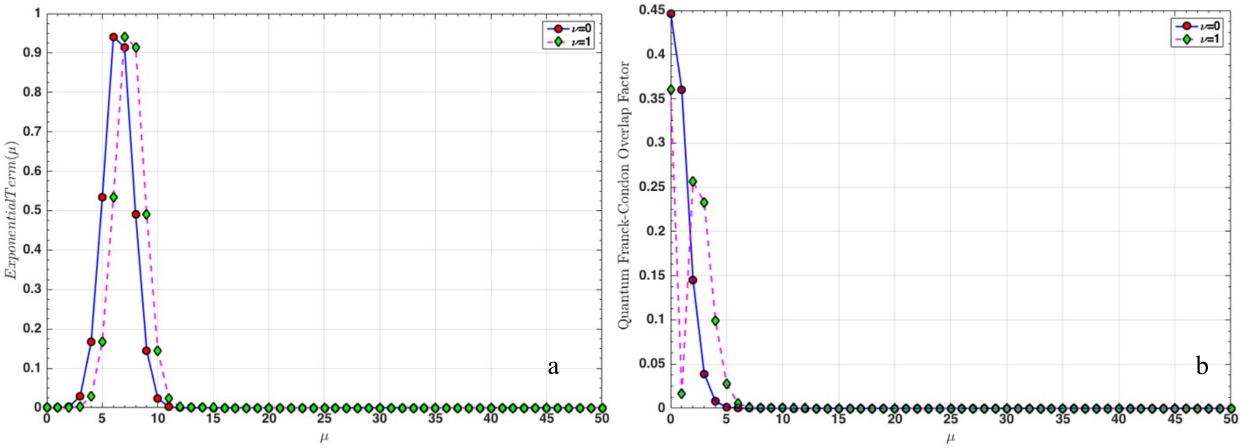

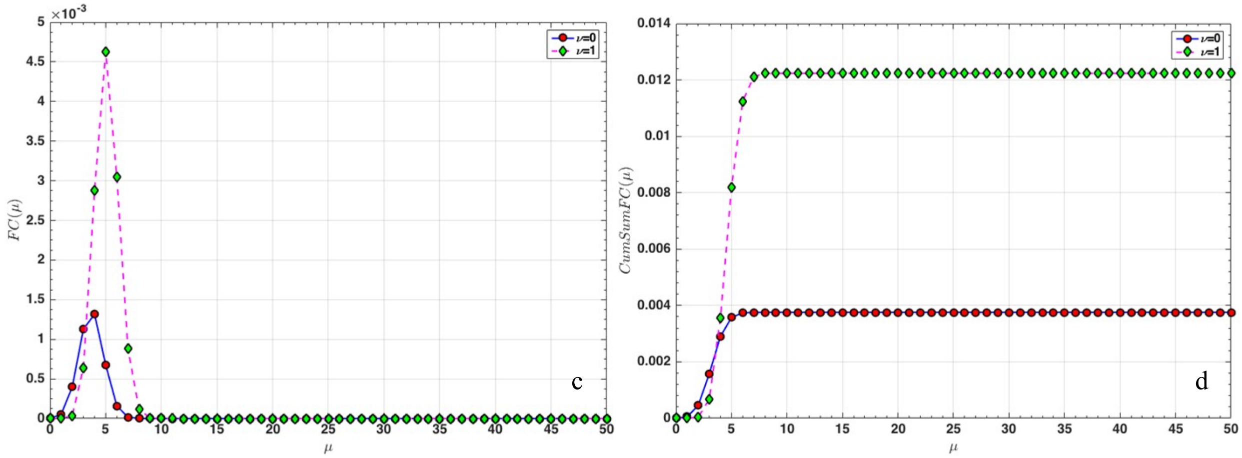

Figure S7. Plot of (a) exponential factors, (b) quantum Franck-Condon overlap factor, (c) Franck-Condon summation factors scaled by $\sqrt{4\lambda_o k_B T}$, and the (d) cumulative sum of terms in the scaled Franck-Condon summation as functions of finial vibrational level μ. Parameters used are: $\lambda_o = 0.60eV$, $\Delta G = -1.4eV$, $\lambda_i = 0.1eV$ and $\hbar\omega = 1000cm^{-1}$.

For a given S ($S \leq 2.5$), the ΔG window width where IR excitation reduces the quantum Franck-Condon factor is ~$0.2 - 0.7eV$ (Table S8). This ΔG window width increase as the Huang-Rhys factor grows. This is because the distance between the two peaks of quantum Franck-Condon overlap factor in $FC_{\nu=1}$ becomes larger as (Fig. S8) when S grows.

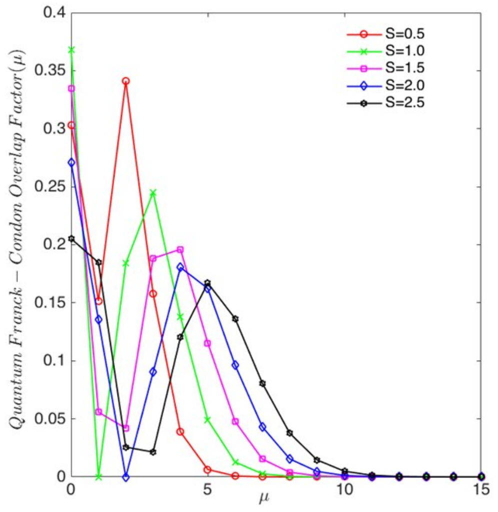

Figure S8 Quantum Franck-Condon overlap distribution in $FC_{\nu=1}$ (see Eq. 6 in main text, quantum Franck-Condon factor is $\frac{e^{-S}S^{\mu-1}}{\mu!}(\mu - S)^2$ when the initial vibrational state $\nu = 1$). As S becomes larger, the value of μ where the quantum Franck-Condon factor reaches its minimum becomes larger and the two peaks are split further apart.

Table S8. Magnitude of the IR-induced maximum rate suppression effect on the Franck-Condon factor and the ΔG window width for different typical value of outer-sphere reorganization energy and Huang-Rhys factor.

	Vibrational Freq. / cm^{-1}	Huang-Rhys Factor	λ_o/ eV		
			0.2	0.4	0.6
Magnitude	500	0.5	1.18	1.09	1.06
		1	1.36	1.18	1.12
		1.5	1.54	1.27	1.18
		2	1.73	1.37	1.24
		2.5	1.91	1.46	1.31
	1000	0.5	1.65	1.34	1.23
		1	2.42	1.7	1.47
		1.5	3.17	2.08	1.72
		2	3.93	2.45	1.97
		2.5	4.68	2.83	2.22
	1700	0.5	2.85	1.93	1.62
		1	7.19	3.13	2.37
		1.5	6.13	4.1	3.09
		2	12.6	5.32	3.82
		2.5	9.61	6.28	4.55
	Vibrational Freq. / cm^{-1}	Huang-Rhys Factor	λ_o/ eV		
			0.2	0.4	0.6
Width / eV	500	0.5	0.23	0.3	0.36
		1	0.24	0.31	0.38
		0.5	0.25	0.33	0.38
		2	0.27	0.33	0.39
		2.5	0.28	0.35	0.4
	1000	0.5	0.26	0.34	0.4
		1	0.32	0.38	0.43
		1.5	0.37	0.41	0.46
		2	0.41	0.45	0.5
		2.5	0.45	0.49	0.53
	1700	0.5	0.34	0.4	0.46
		1	0.48	0.51	0.55
		1.5	0.59	0.6	0.63
		2	0.65	0.68	0.71
		2.5	0.69	0.74	0.77

III.4. IR INDUCED CHANGES TO THE CLASSICAL (MARCUS) FRANCK-CONDON FACTOR

The non-adiabatic ET rate, following Eqs. 53 and 65 in Ref. [20], can be written as

(S10)

$$k_{ET} = \langle transition\ velocity \rangle \cdot \langle density\ of\ state\ at\ curve\ crossin$$

(S11)

$$= \frac{1}{2} \langle |\dot{\xi}(t)| \Upsilon[\dot{\xi}(t)] \rangle_{\dot{\xi}} \langle \delta(\xi(t) - \xi_c) \rangle_{\xi}$$

$$= \frac{1}{2} \left[\int_0^{\sqrt{\frac{2E}{m}}} \frac{|\dot{\xi}(t)| \cdot 4\pi H_{DA}^2}{\hbar |\dot{\xi}(t)| |s_D - s_A|} \wp[|\dot{\xi}(t)|] d|\dot{\xi}(t)| \right] \left[\frac{\omega}{\pi} \int_{-\infty}^{+\infty} d\xi \delta(\xi - \xi_x) \int_0^{+\infty}$$

(S12)

$$= \frac{2\pi H_{DA}^2}{\hbar} \cdot \frac{1}{\omega\sqrt{2\lambda m}\pi} \frac{\omega}{} \sqrt{\frac{m}{2}} \int_0^{+\infty} dE \frac{1}{\sqrt{E - \Delta G^{\neq}}} H(E - \Delta G^{\neq}) \rho(E)$$

(S13)

$$= \frac{H_{DA}^2}{\hbar} \frac{1}{\sqrt{\lambda}} \int_0^{+\infty} dE \frac{1}{\sqrt{E - \Delta G^{\neq}}} H(E - \Delta G^{\neq}) \rho(E)$$

(S14)

Here $\dot{\xi}(t)$ is the nuclear velocity, $\Upsilon[\dot{\xi}(t)]$ is the Landau-Zener transition probability at the curve crossing and m is the reduced mass. s_D and s_A are the slope of potential energy surface at curve crossing for donor and acceptor surfaces, respectively. $\wp[|\dot{\xi}(t)|]$ is the probability distribution function of nuclear velocity. ω is the reaction coordinate vibrational frequency, ξ is the reaction coordinate, ξ_x is the ξ value at curve crossing. $V(\xi)$ describes the potential energy surface and at ξ_x, $V(\xi_x) = \Delta G^{\neq}$. λ is the total reorganization energy, m is the reduced mass, E is the total energy of the reaction coordinate, $\rho(E)$ is the probability distribution function of E, and H is the Heaviside step function. The difference between equilibrium and nonequilibrium ET rate is

$$k_{ET}^{neq} - k_{ET}^{eq} = \frac{H_{DA}^2}{\hbar} \frac{1}{\sqrt{\lambda}} \int_0^{+\infty} dE \frac{1}{\sqrt{E - \Delta G^{\neq}}} H(E - \Delta G^{\neq}) [\rho_{neq}(E) - \rho_{eq}(E)] \tag{S15}$$

where $\rho_{eq}(E)$ and $\rho_{neq}(E)$ stands for equilibrium and nonequilibrium energy distribution, respectively. The difference between $\rho_{eq}(E)$ and $\rho_{neq}(E)$ is produced by IVR, therefore we can approximate the IVR-induced change of energy distribution as

$$\rho_{neq}(E) - \rho_{eq}(E) = \sum_{E_i = 0,\ E_i < E_j} \Delta\rho(E_i, E_j) [\delta(E = E_j) - \delta(E = E_i)] \tag{S16}$$

Here, $\Delta\rho(E_i,E_j)$ is the probability density moved from $E = E_i$ to $E = E_j$ by IVR. Because IVR injects vibrational energy into reaction coordinate, the flux from lower energies to higher energies is much larger than the flux from higher energies to lower energies.[21] Thus, here we ignore the $\Delta\rho(E_i,E_j)$ moved from higher energies to lower energies ($E_i > E_j$). In the case of near activationless ET ($\Delta G \approx 0$), the IVR increases the value of $\rho(E)$ at higher energies, leading to a decrease of ET rate ($\frac{1}{\sqrt{E_j}} < \frac{1}{\sqrt{E_i}}$ when $E_j > E_i$). In the case of highly activated ET, before IVR-excitation, $k_{ET}^{eq} \approx 0$ since $\rho(E \approx \Delta G^{\neq}) \approx 0$. IVR may produce $\Delta\rho(E_i,E_j)$ where $E_i < \Delta G^{\neq} < E_j$, leading to a non-vanishing k_{ET}^{neq}. Hence for highly activated ET reactions, IVR-excitation of classical reaction coordinate may accelerate ET rates.

By replacing $\rho_{eq}(E)$ with Boltzmann distribution ($\rho_{eq}(E) = \frac{1}{k_BT}\exp\left[-\frac{E}{k_BT}\right]$), one can recover the Marcus' classical ET rate expression. Therefore, nonequilibrium ET rate can be written as

$$k_{ET}^{neq} = \frac{H_{DA}^2}{\hbar}\frac{1}{\sqrt{\lambda}}\left[\sqrt{\frac{\pi}{k_BT}}\exp\left[-\frac{\Delta G^{\neq}}{k_BT}\right] + \int_0^{+\infty} dE\frac{1}{\sqrt{E-\Delta G^{\neq}}}H(E-\Delta G^{\neq})\sum_{E_i=0,\ E_i<E_j}\Delta\rho(E_i,E_j)\left[\delta(E=E_j)-\delta(E=E_i)\right]\right] \qquad \text{(S17)}$$

This nonequilibrium rate expression can be effectively expressed as a simple ET rate form with a shifted activation free energy ($\Delta G^{\neq} + \delta G^{\neq}$) as

$$k_{ET}^{neq} = \frac{2\pi}{\hbar}H_{DA}^2\frac{1}{\sqrt{4\pi\lambda k_BT}}\exp\left[-\frac{\Delta G^{\neq} + \delta G^{\neq}}{k_BT}\right] \qquad \text{(S18)}$$

REFERENCE:

1. Naraharisetty, S. R. G.; Kurochkin, D. V.; Rubtsov, I. V., C-D Modes as Structural Reporters via Dual-Frequency 2DIR Spectroscopy. *Chem. Phys. Lett.* **2007,** *437*, 262-266.

2. Kurochkin, D. V.; Naraharisetty, S. R. G.; Rubtsov, I. V., Dual-Frequency 2D IR on Interaction of Weak and Strong IR Modes. *J. Phys. Chem. A* **2005,** *109*, 10799-10802.

3. Sessler, J. L.; Sathiosatham, M.; Brown, C. T.; Rhodes, T. A.; Wiederrecht, G., Hydrogen-Bond-Mediated Photoinduced Electron-Transfer: Novel Dimethylaniline-Anthracene Ensembles Formed via Watson-Crick Base-Pairing. *J. Am. Chem. Soc.* **2001,** *123*, 3655-3660.

4. Sessler, J. L.; Sathiosatham, M.; Brown, C. T.; Rhodes, T. A.; Wiederrecht, G., Hydrogen-bond-mediated photoinduced electron-transfer: Novel dimethylaniline-anthracene ensembles formed via Watson-Crick base-pairing. *J. Am. Chem. Soc.* **2001,** *123*, 3655-3660.

5. Frisch, M. J. T., G. W.; Schlegel, H. B.; Scuseria, G. E.; Robb, M. A.; Cheeseman, J. R.; Scalmani, G.; Barone, V.; Mennucci, B.; Petersson, G. A.; Nakatsuji, H.; Caricato, M.; Li, X.; Hratchian, H. P.; Izmaylov, A. F.; Bloino, J.; Zheng, G.; Sonnenberg, J. L.; Hada, M.; Ehara, M.; Toyota, K.; Fukuda, R.; Hasegawa, J.; Ishida, M.; Nakajima, T.; Honda, Y.; Kitao, O.; Nakai, H.; Vreven, T.; Montgomery, J. A., Jr.; Peralta, J. E.; Ogliaro, F.; Bearpark, M.; Heyd, J. J.; Brothers, E.; Kudin, K. N.; Staroverov, V. N.; Kobayashi, R.; Normand, J.; Raghavachari, K.; Rendell, A.; Burant, J. C.; Iyengar, S. S.; Tomasi, J.; Cossi, M.; Rega, N.; Millam, J. M.; Klene, M.; Knox, J. E.; Cross, J. B.; Bakken, V.; Adamo, C.; Jaramillo, J.; Gomperts, R.; Stratmann, R. E.; Yazyev, O.; Austin, A. J.; Cammi, R.; Pomelli, C.; Ochterski, J. W.; Martin, R. L.; Morokuma, K.; Zakrzewski, V. G.; Voth, G. A.; Salvador, P.; Dannenberg, J. J.; Dapprich, S.; Daniels, A. D.; Farkas, Ö.; Foresman, J. B.; Ortiz, J. V.; Cioslowski, J.; Fox, D. J. *Gaussian 09, Revision D.01*, Gaussian, Inc.: Wallingford CT, 2009.

6. Lin, Z. W.; Lawrence, C. M.; Xiao, D. Q.; Kireev, V. V.; Skourtis, S. S.; Sessler, J. L.; Beratan, D. N.; Rubtsov, I. V., Modulating Unimolecular Charge Transfer by Exciting Bridge Vibrations. *J. Am. Chem. Soc.* **2009,** *131*, 18060-18062.

7. Senthilkumar, K.; Grozema, F. C.; Bickelhaupt, F. M.; Siebbeles, L. D. A., Charge Transport in Columnar Stacked Triphenylenes: Effects of Conformational Fluctuations on Charge Transfer Integrals and Site Energies. *J. Chem. Phys.* **2003,** *119*, 9809-9817.

8. Senthilkumar, K.; Grozema, F. C.; Guerra, C. F.; Bickelhaupt, F. M.; Lewis, F. D.; Berlin, Y. A.; Ratner, M. A.; Siebbeles, L. D. A., Absolute Rates of Hole Transfer in DNA. *J. Am. Chem. Soc.* **2005,** *127*, 14894-14903.

9. *ADF2016*, SCM, Theoretical Chemistry, Vrije Universiteit: Amsterdam, The Netherland, 2016.

10. Cave, R. J.; Newton, M. D., Generalization of the Mulliken-Hush Treatment for the Calculation of Electron Transfer Matrix Elements. *Chem. Phys. Lett.* **1996,** *249*, 15-19.

11. Cave, R. J.; Newton, M. D., Calculation of Electronic Coupling Matrix Elements for Ground and Excited State Electron Transfer Reactions: Comparison of the Generalized Mulliken-Hush and Block Diagonalization Methods. *J. Chem. Phys.* **1997,** *106*, 9213-9226.

12. Subotnik, J. E.; Yeganeh, S.; Cave, R. J.; Ratner, M. A., Constructing Diabatic States from Adiabatic States: Extending Generalized Mulliken-Hush to Multiple Charge Centers with Boys Localization. *J. Chem. Phys.* **2008,** *129*.

13. Nelsen, S. F.; Blackstock, S. C.; Kim, Y., Estimation of Inner Shell Marcus Terms for Amino Nitrogen-Compounds by Molecular-Orbital Calculations. *J. Am. Chem. Soc.* **1987,** *109*, 677-682.

14. Reimers, J. R., A Practical Method for the Use of Curvilinear Coordinates in Calculations of Normal-Mode-Projected Displacements and Duschinsky Rotation Matrices for Large Molecules. *J. Chem. Phys.* **2001,** *115*, 9103-9109.

15. Kühn, O. M., Volkhard, *Charge and Energy Transfer Dynamics in Molecular Systems*. 3rd ed.; Wiley-VCH: Berlin, 2011.

16. Skourtis, S. S.; Balabin, I. A.; Kawatsu, T.; Beratan, D. N., Protein Dynamics and Electron Transfer: Electronic Decoherence and Non-Condon Effects. *Proc. Natl. Acad. Sci. U.S.A.* **2005,** *102*, 3552-3557.

17. Skourtis, S. S.; Waldeck, D. H.; Beratan, D. N., Fluctuations in Biological and Bioinspired Electron-Transfer Reactions. *Annu. Rev. Phys. Chem.* **2010,** *61*, 461-485.

18. Troisi, A.; Nitzan, A.; Ratner, M. A., A Rate Constant Expression for Charge Transfer Through Fluctuating Bridges. *J. Chem. Phys.* **2003,** *119*, 5782-5788.

19. Ulstrup, J.; Jortner, J., Effect of Intramolecular Quantum Modes on Free-Energy Relationships for Electron-Transfer Reactions. *J. Chem. Phys.* **1975,** *63*, 4358-4368.

20. Sumi, H., Adiabatic versus Non-Adiabatic Electron Transfer. In *Electron Transfer in Chemistry*, Wiley-VCH Verlag GmbH: 2008; pp 64-108.

21. Burin, A. L.; Tesar, S. L.; Kasyanenko, V. M.; Rubtsov, I. V.; Rubtsov, G. I., Semiclassical Model for Vibrational Dynamics in Polyatomic Molecules: Investigation of Internal Vibrational Relaxation. *J. Phys. Chem. C* **2010,** *114*, 20510-20517.